Supporting Information

Structural explanation of the dielectric enhancement of barium titanate nanoparticles grown under hydrothermal conditions

Ana F. Suzana[*], *Sizhan Liu, Jiecheng Diao, Longlong Wu, Tadesse A. Assefa*[†], *Milinda Abeykoon, Ross Harder, Wonsuk Cha, Emil S. Bozin, and Ian K. Robinson*[*]

BCDI technique

Bragg coherent diffraction imaging (BCDI) is a lens-less imaging technique explored over the last 20 years mainly due to the development of the coherence properties of X-rays delivered in third/fourth-generation synchrotrons[1] and, more recently, X-ray free-electron laser (XFEL)[2] facilities. The low emittance of the radiation, characteristic of these machines, coupled with high-quality focusing optics leads to a small-sized focused coherent X-ray beam capable of illuminating one single nanocrystal. In BCDI, if the beam is coherent in both longitudinal and transverse directions, it is possible to know the phase shift of the diffracted beam caused by atomic-scale displacements in the crystalline structure of the single isolated nanocrystals, as established by equation (1).[3] Therefore, the technique is sensitive to atomic displacements and one can reconstruct in 3D the electron density and the displacement field of a nanocrystal, if the oversampling criterion is met[4]. A deeper discussion on the characterization of nanocrystals using coherent X-ray sources can be found elsewhere.[3,5] This technique has been used to probe the displacement field distribution of several systems under *in situ* conditions, including catalytic processes[6,7], cathode/anode materials under working conditions (charging/discharging)[8–10], and crystal growth and dissolution processes.[11] BCDI has also been applied to characterize BTO nanocrystals[12,13].

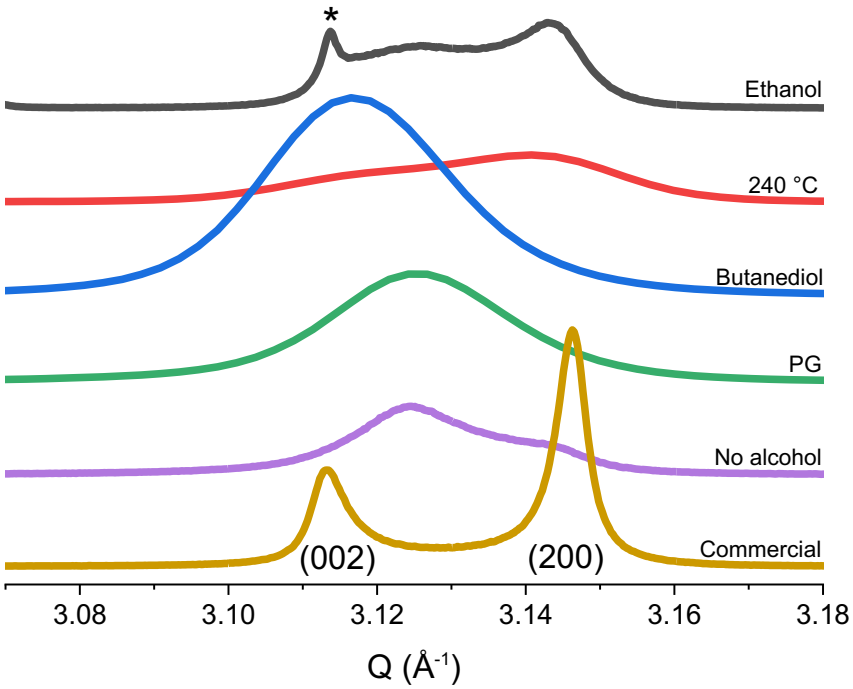

Figure S1. XRD patterns showing the (002)/(200) enlarged region of the samples synthesized by the hydrothermal approach. The commercial tetragonal sample was included in the plot.

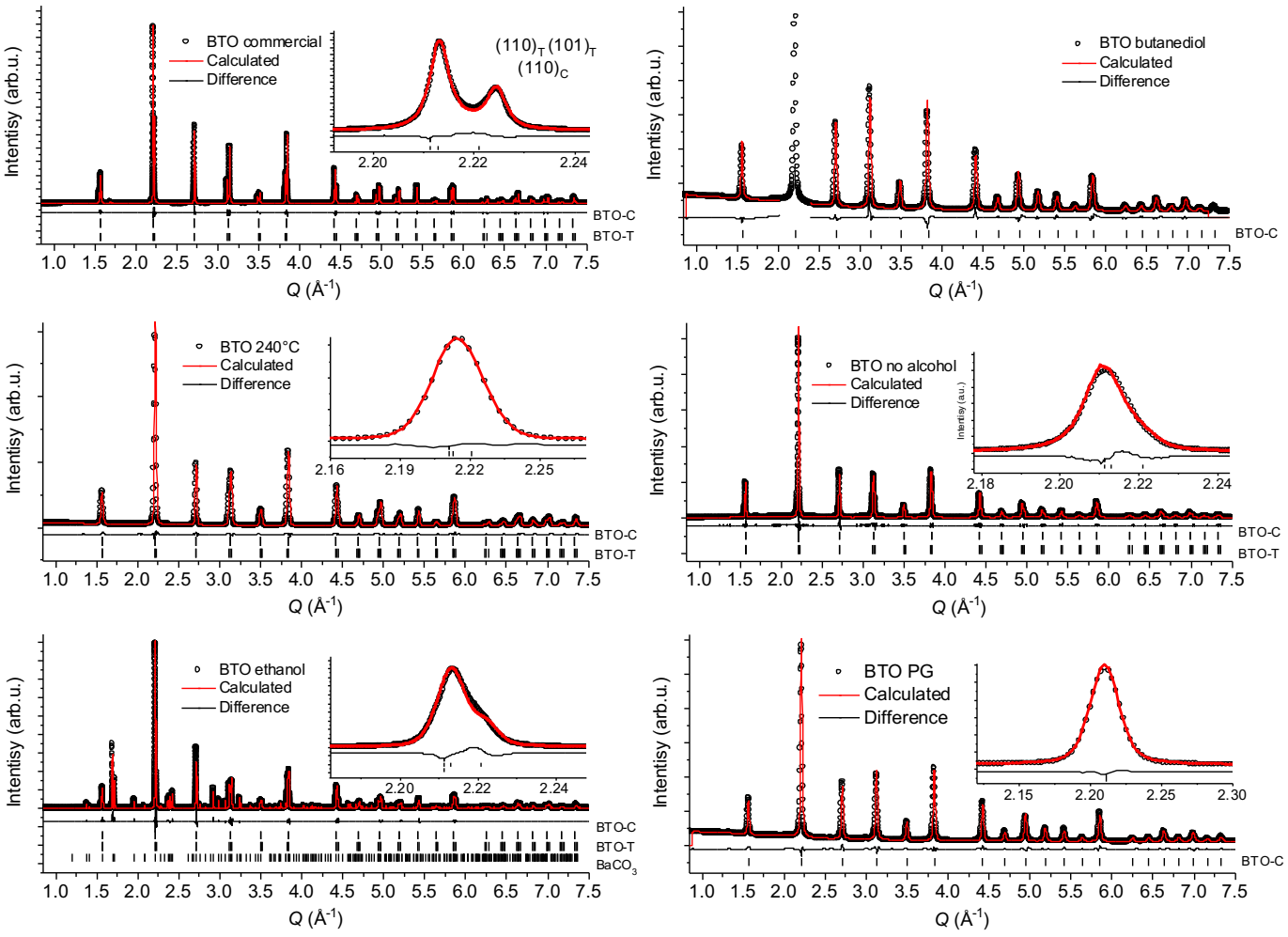

Figure S2. Rietveld refinement of the XRD patterns shown in Figure 2 of the main text. The result of the refinement is shown as a red solid line, and the difference function, as a black solid line. The inset in the plots show the (110)/(101) peaks, which are split when tetragonal phase is present. The inset is not displayed for the sample BTO butanediol because this peak was saturated and excluded from the refinement.

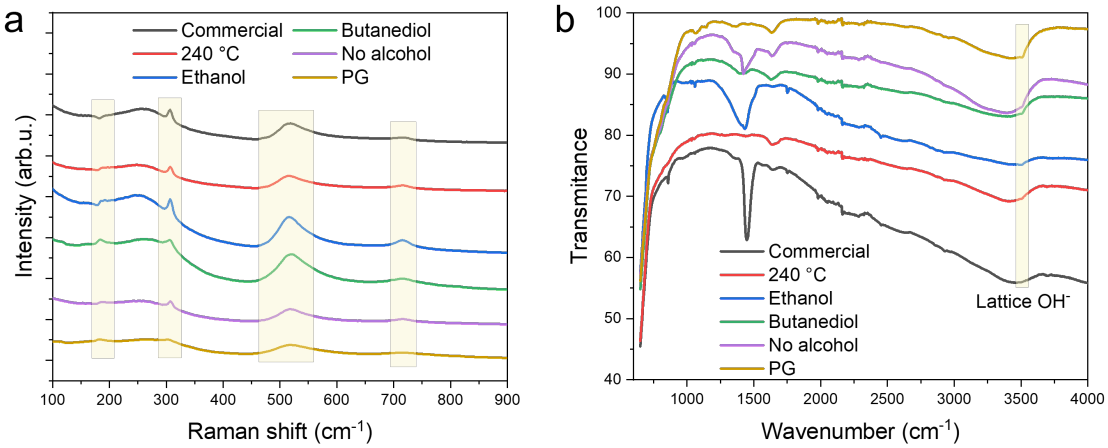

Figure S3. (a) Raman spectra of the BTO powders. The bands highlighted in the yellow boxes (185, 310, 515 and 715 cm^{-1}) are originating from the tetragonal structure of BTO. (b) FTIR spectra of the BTO samples synthesized under different conditions, and the commercial sample. All the samples were thermally treated for 20 h at 120 °C in order to avoid surface OH^- groups coming from water.

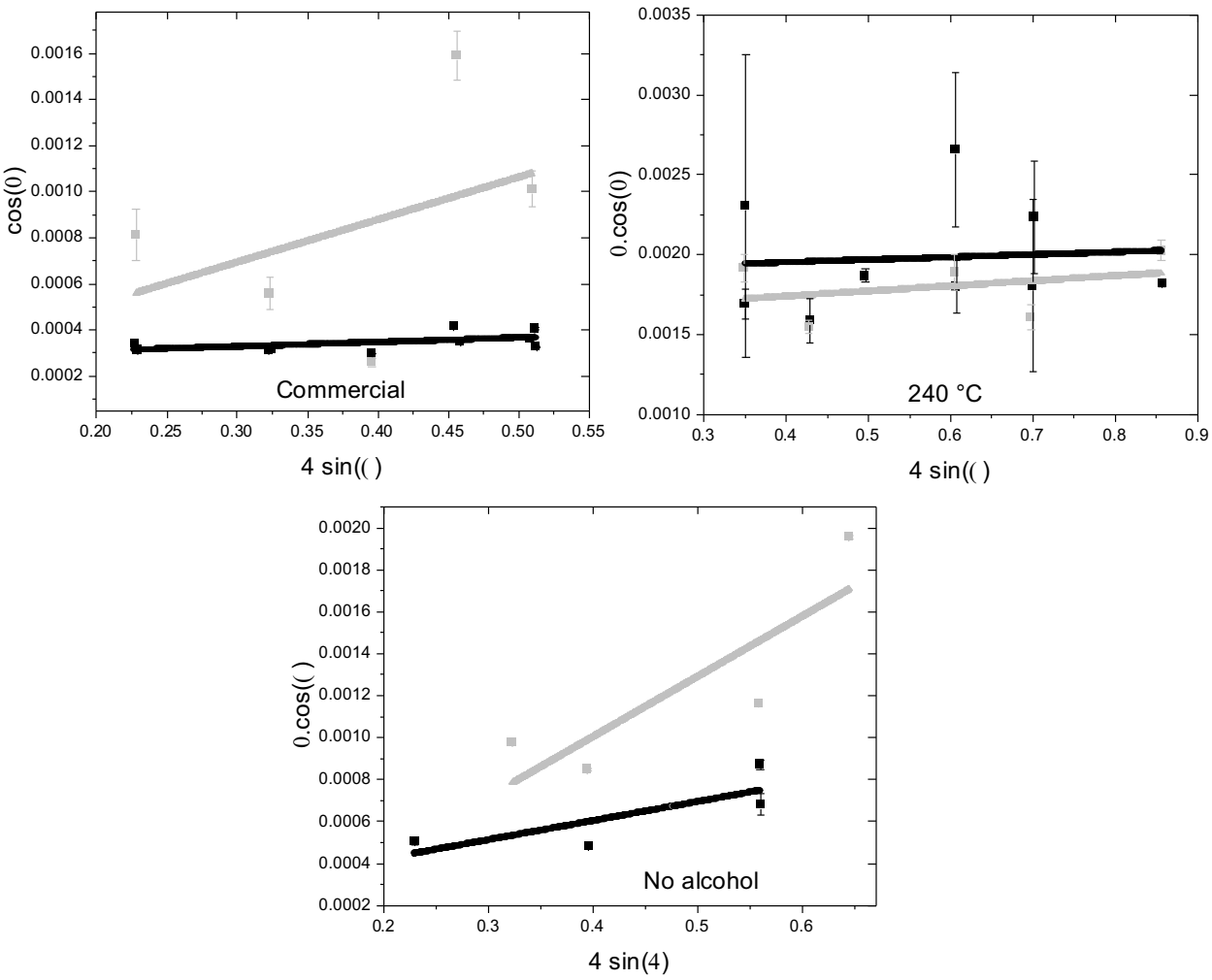

Figure S4. Williamson-Hall plots for the samples commercial, 240 °C, and no alcohol. The straight lines represent the linear fits for each sample. The reflections indexed as cubic phase were plotted in gray, and the tetragonal symmetry peaks are shown in black.

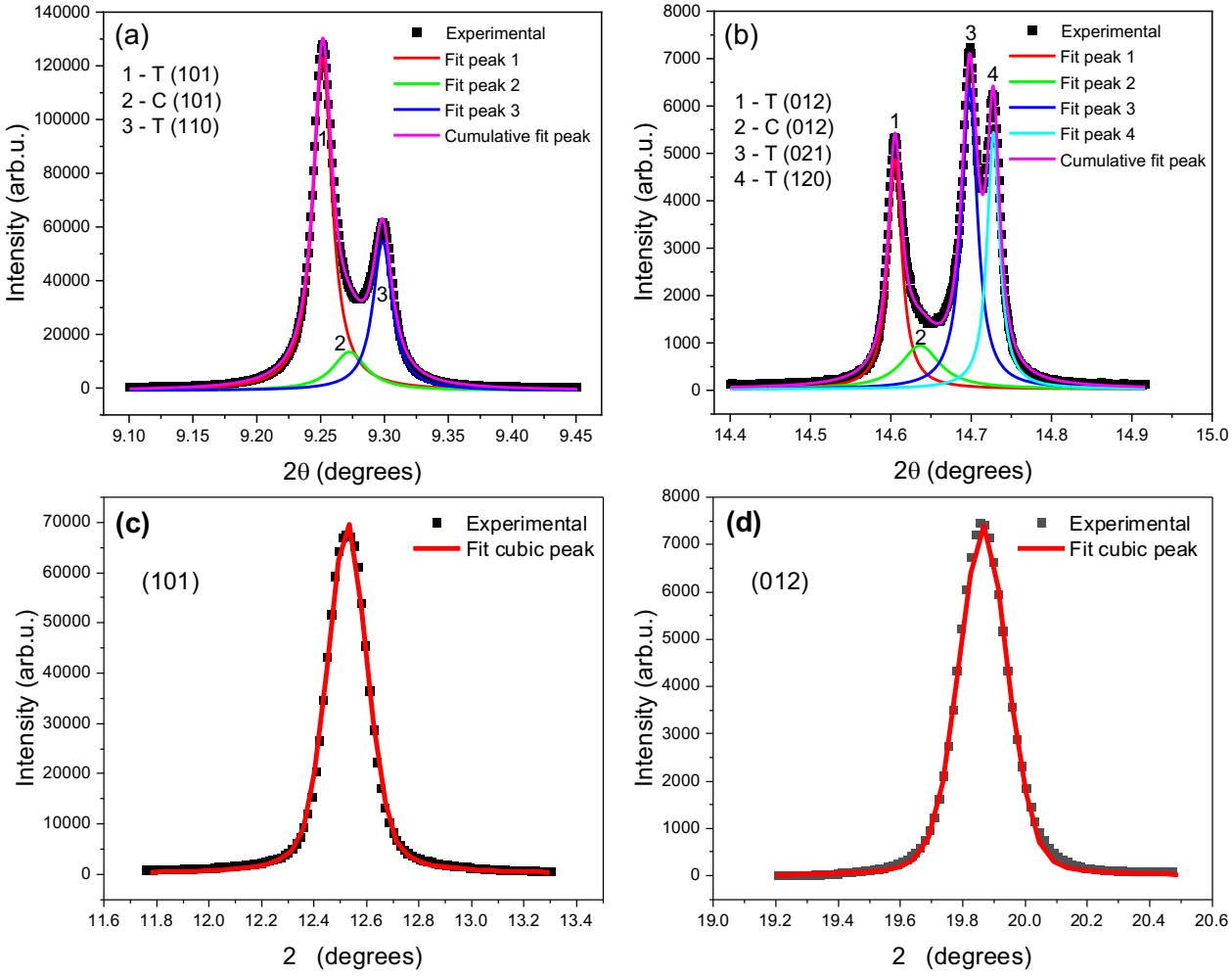

Figure S5. Example of the peak fitting done for the Williamson-Hall approach for the samples BTO commercial (a,b) and BTO butanediol (c,d). (a) Lorentzian function fit for the (101) and (110) tetragonal reflections (peaks 1 and 3) and (101) cubic reflection (peak 2). (b) the same for the peaks (012), (021), and (120) tetragonal reflections (peaks 1, 3, and 4) and (012) cubic reflection (peak 2). (c) Fit for the (101) reflection and (d) for the (012). T and C stand for tetragonal and cubic phases, respectively.

Table S1. PDF fit residuals r_w (%) and tetragonal distortion (t) for the fits done over 1.2-80Å range.

Model	Sample

	commercial	240 °C	ethanol	butanediol	no alcohol	PG
cubic	19	16	15	18	14	14
tetragonal	9	10	10	9	11	11
t	0.015(2)	0.015(2)	0.016(2)	0.016(2)	0.013(2)	0.013(2)

Table S2. PDF fit residuals r_w (%) and tetragonal distortion (t) for the fits done over 1.2-10 Å range.

Model \ Sample	commercial	240 °C	ethanol	butanediol	no alcohol	PG
cubic	14	14	14	12	13	12
tetragonal	9.7	9.8	10	9.8	8.8	9.4
t	0.014(1)	0.014(1)	0.014(1)	0.014(1)	0.013(1)	0.011(1)
orthorhombic	9.7	10	10	8.5	8.5	8.6
rhombohedral	16	10	12	9.3	9.8	9.4

Table S3. Size and inhomogeneous strain components extracted from the Williamson-Hall plot $\beta_{tot}\ cos\theta$ versus 4 $sin\theta$ for the BTO samples synthesized through the hydrothermal approach and the commercial sample. C and T denote cubic and tetragonal phases, respectively.

Sample	Intercept (10^{-4})	Size (nm)	Inhomogeneous strain (slope) (10^{-4})
BTO commercial	C: 1.4 T: 2.7	C: 293.2 T: 153.3	C: 18.4 T: 1.9
BTO-240 °C	C: 16.1 T: 18.8	C: 27.7 T: 23.7	C: 3.2 T: 5.8
BTO ethanol	C: -2.6 T: 3.4	C: - T: 102	C: 17.3 T: 7.6
BTO butanediol	17.4	32	21.7
BTO no alcohol	C: 1.4 T: 9.1	C: - T: 45	C: 28.7 T: 2.37
BTO PG	17.0	33	14.9

References

1. D., Shi, X. Reininger, Harder, R., Haeffner, R. X-ray optics simulation and beamline design for the APS upgrade. *Advances in Computational Methods for X-Ray Optics IV*; **2017**, *103880*, 1-12.
2. Yun, K., Kim, S., Kim, D., Chung, M., Jo, W., Hwang, H., Nam, D., Kim, S., Kim, J., Park, S., Kim, K. S., Song, C., Lee, S., Kim, H. Coherence and pulse duration characterization of the PAL-XFEL in the hard X-ray regime. *Sci. Rep.* **2019**, *9*, 1–7.
3. Robinson, I. Nanoparticle Structure by coherent X-ray diffraction. *J. Phys. Soc. Japan* **2013**, *82*, 1–7.
4. Miao, J., Sayre, D. On possible extensions of X-ray crystallography through diffraction-pattern oversampling. *Acta Crystallogr. Sect. A Found. Crystallogr.* **2000**, *56*, 596–605.
5. Robinson, I., Harder, R. Coherent X-ray diffraction imaging of strain at the nanoscale.

Nat. Mater. **2009**, *8*, 291–298.
6. Suzana, A. F., Rochet, A., Passos, A. R., Zerba, J. P. C., Polo, C. C., Santilli, C. V., Pulcinelli, S. H., Berenguer, F., Harder, R., Maxey, E., Meneau, F. In situ three-dimensional imaging of strain in gold nanocrystals during catalytic oxidation. *Nanoscale Adv.* **2019**, *1*, 3009–3014.
7. Kim, D., Chung, M., Carnis, J., Kim, S., Yun, K., Kang, J., Cha, W., Cherukara, M. J., Maxey, E., Harder, R., Sasikumar, K., Sankaranarayanan, S. K. R. S., Zozulya, A., Sprung, M., Riu, D., Kim, H. Active site localization of methane oxidation on Pt nanocrystals. *Nat. Commun.* **2018**, *9*, 1–7.
8. Estandarte, A. K. C., Diao, J., Llewellyn, A. V., Jnawali, A., Heenan, T. M. M., Daemi, S. R., Bailey, J. J., Cipiccia, S., Batey, D., Shi, X., Rau, C., Brett, D. J. L., Jervis, R., Robinson, I. K., Shearing, P. R. Operando Bragg Coherent Diffraction Imaging of $LiNi_{0.8}Mn_{0.1}Co_{0.1}O_2$ Primary Particles within Commercially Printed NMC811 Electrode Sheets. *ACS Nano* **2021**, *15*, 1321–1330.
9. Ulvestad, A., Singer, A., Clark, J. N., Cho, H. M., Kim, J. W., Harder, R., Maser, J., Meng, Y. S. & Shpyrko, O. G. Topological defect dynamics in operando battery nanoparticles. *Science* **2015**, *348*, 1344–1347.
10. Assefa, T. A., Suzana, A. F., Wu, L., Koch, R. J., Li, L., Cha, W., Harder, R., Bozin, E. S., Wang, F., Robinson, I. K. Imaging the Phase Transformation in Single Particles of the Lithium Titanate Anode for Lithium-Ion Batteries. *ACS Appl. Energy Mater.* **2021**, *4*, 111–118.
11. Clark, J. N., Ihli, J., Schenk, A. S., Kim, Y., Kulak, A. N., Campbell, J. M., Nisbet, G., Meldrum, F. C. & Robinson, I. K. Three-dimensional imaging of dislocation propagation during crystal growth and dissolution. *Nat. Mater.* **2015**, *14*, 780-784.
12. Diao, J., Shi, X., Assefa, T. A., Wu, L., Suzana, A. F., Nunes, D. S., Batey, D., Cipiccia, S., Rau, C., Harder, R., Cha, W., Robinson, I. K. Evolution of ferroelastic domain walls during phase transitions in barium titanate nanoparticles. *Phys. Rev. Mater.* **2020**, *4*, 1–8.
13. Karpov, D., Liu, Z., Rolo, T. S., Harder, R., Balachandran, P. V., Xue, D., Lookman, T. & Fohtung, E. Three-dimensional imaging of vortex structure in a ferroelectric nanoparticle driven by an electric field. *Nat. Commun.* **2017**, *8*, 1–7.